photonics

MDPI

Article

Brillouin Zone Folding-Induced Magnetic Toroidal Dipole Metasurfaces for Tunable Mid-Infrared Upconversion

Wanghao Zhu [1,2], Congfu Zhang [1,2], Wenjuan Shi [1], Di Ma [1,2] and Hongjun Liu [1,3,*]

[1] State Key Laboratory of Ultrafast Optical Science and Technology, Xi'an Institute of Optics and Precision Mechanics, Chinese Academy of Sciences, Xi'an 710119, China; zhuwanghao23@mails.ucas.ac.cn (W.Z.); zhangcongfu@opt.ac.cn (C.Z.); shiwenjuan@opt.ac.cn (W.S.); madi23@mails.ucas.ac.cn (D.M.)
[2] University of Chinese Academy of Sciences, Beijing 100084, China
[3] Collaborative Innovation Center of Extreme Optics, Shanxi University, Taiyuan 030006, China
* Correspondence: liuhongjun@opt.ac.cn

Abstract

High quality factor (Q factor) resonant metasurfaces enable efficient mid-infrared (MIR) upconversion, yet their narrow operating bandwidths severely limit practical broadband detection and imaging applications. Although high Q magnetic toroidal dipole (MTD) modes exhibit outstanding momentum space (*k*-space) stability in linear optics, their application in nonlinear processes has primarily been confined to degenerate second-harmonic generation (SHG), leaving complex non-degenerate processes such as sum-frequency generation (SFG) largely unexplored. Here, we propose a tunable MIR upconversion platform based on an all-dielectric gallium phosphide (GaP) dimer metasurface. Breaking the in-plane symmetry to trigger Brillouin zone folding excites robust MTD quasi-guided modes (MTD-QGM), tightly confining the locally enhanced optical fields within the highly nonlinear GaP nanostructure. Synchronizing this high Q resonance with a spatially overlapping pump mode yields an exceptional SFG conversion efficiency of 7.9×10^{-4}, successfully translating a 3101.8 nm MIR signal to the 903 nm near-infrared band. Crucially, the intrinsic *k*-space stability of the MTD-QGM enables continuous, broadband upconversion through simple angle tuning. This mechanism effectively overcomes the narrow-band limitations characteristic of typical symmetry-protected resonators, establishing a robust paradigm for room-temperature MIR detection.

Keywords: metasurface; sum-frequency generation (SFG); nonlinear optics

1. Introduction

The mid-infrared (MIR) spectral range, particularly the 3–5 μm atmospheric window, is of paramount importance for numerous applications, including molecular fingerprint spectroscopy, environmental monitoring, and imaging [1–3]. Despite its significance, traditional MIR detectors typically require cryogenic cooling to suppress thermal noise, resulting in bulky and complex systems [4]. Frequency upconversion technology offers an elegant solution by translating MIR signals into the near-infrared (NIR) or visible regime via nonlinear parametric processes, enabling room-temperature detection using mature silicon-based CMOS sensors [5]. While macroscopic nonlinear crystals are conventionally employed for this purpose, they are inherently constrained by stringent phase-matching requirements. All-dielectric metasurfaces have emerged as a compelling alternative, fundamentally relaxing these phase-matching constraints. In stark contrast to plasmonic nanostructures [6], high-refractive-index dielectric metasurfaces significantly mitigate non-radiative Ohmic

Check for updates

Received: 12 March 2026
Revised: 1 April 2026
Accepted: 2 April 2026
Published: 7 April 2026

Copyright: © 2026 by the authors. Licensee MDPI, Basel, Switzerland. This article is an open access article distributed under the terms and conditions of the Creative Commons Attribution (CC BY) license.

losses while simultaneously supporting strong electric and magnetic multipolar resonances, establishing an ideal platform for nanoscale nonlinear frequency conversion [7–9].

In nonlinear metasurfaces, the strategic engineering of multipolar resonances is crucial for maximizing local optical field enhancement [10]. Traditionally, the optical responses of most all-dielectric metasurfaces have been dominated by conventional electric dipoles (ED) and magnetic dipoles (MD) [11–13], whereas toroidal dipoles (TD) have historically been overlooked due to their significantly weaker scattering responses [14,15]. However, high quality factor (Q factor) TD resonances have recently attracted intense interest due to their unparalleled ability to tightly squeeze electromagnetic energy into ultra-confined volumes, substantially boosting light–matter interactions [16–18]. Nevertheless, the vast majority of reported TD are electric toroidal dipoles (ETD), where the strongly enhanced electric fields are predominantly localized within low-index air gaps or nanoholes. Conversely, magnetic toroidal dipoles (MTD) offer distinct advantages: by supporting anti-rotating magnetic vortices that induce head-to-tail electric dipoles, MTD tightly confine the enhanced electric fields within the high-refractive-index dielectric structures [19–21]. This characteristic renders MTD highly promising candidates for enhancing nonlinear upconversion.

To fully harness these internal localized fields for nonlinear processes, achieving high Q factors is imperative. Currently, the mainstream approach relies on symmetry-protected bound states in the continuum (BICs). By introducing symmetry breaking, BICs can be transformed into quasi-BICs (QBICs) [22–27]. However, the high Q resonances of QBICs exist only within a highly restricted region near the BIC in momentum space (*k*-space). To bypass this bottleneck, quasi-guided modes (QGM) induced by Brillouin zone folding emerge as a highly robust alternative [28–31]. By engineering the period doubling of the metasurface lattice, guided modes (GMs) below the light line are folded back to the Γ point, generating high Q resonances that exhibit exceptional *k*-space stability, thereby compensating for the intrinsic angular limitations of typical BICs. Concurrently, while recent studies have explored MTD in non-centrosymmetric lithium niobate platforms to enhance second-harmonic generation (SHG) [32], these pioneering explorations are primarily restricted to degenerate processes involving a single incident beam. For MIR detection, sum-frequency generation (SFG) is urgently required. As a fundamentally more complex, non-degenerate three-wave mixing process, which strictly couples only the incident pump and signal fields to produce a single sum-frequency output, without the involvement of an idler wave, SFG dictates the simultaneous excitation of two independent optical fields and the realization of their precise spatial mode overlap. Achieving this dual-mode overlap to enable continuous, broadband upconversion remains a formidable challenge.

In this study, we extend this approach to the highly second-order nonlinear III-V semiconductor Gallium Phosphide (GaP) to tackle the challenge of broadband MIR upconversion [33–35]. By breaking the in-plane translational symmetry of GaP nanorod dimers, we realize Brillouin zone folding to excite the robust magnetic toroidal dipole quasi-guided modes (MTD-QGM). Utilizing the unique internal field confinement of the MTD, we successfully achieve a spatial mode overlap with a precisely synchronized pump resonance. Consequently, we demonstrate a remarkably high SFG conversion efficiency of 7.9×10^{-4}, translating a 3101.8 nm MIR signal to the 903 nm NIR band. Crucially, capitalizing on the intrinsic k-space stability of the MTD-QGM, our metasurface supports continuous, angle-tunable broadband MIR upconversion without sacrificing conversion efficiency, elegantly bypassing the inherent narrow-band limitations of typical QBICs resonance.

2. Metasurface Structural Design

Our proposed metasurface comprises an array of GaP nanorod dimers supports on a silicon dioxide (SiO_2) substrate, as illustrated in Figure 1a. The excitation mechanism of

the MTD is depicted in Figure 1c. As the spacing between the two constituent nanorods varies, each nanorod sustains an anti-rotating magnetic vortex, subsequently giving rise to head-to-tail electric dipoles. Ultimately, this distinctive electromagnetic field topology excites the MTD mode oriented along the axis between the nanorods.

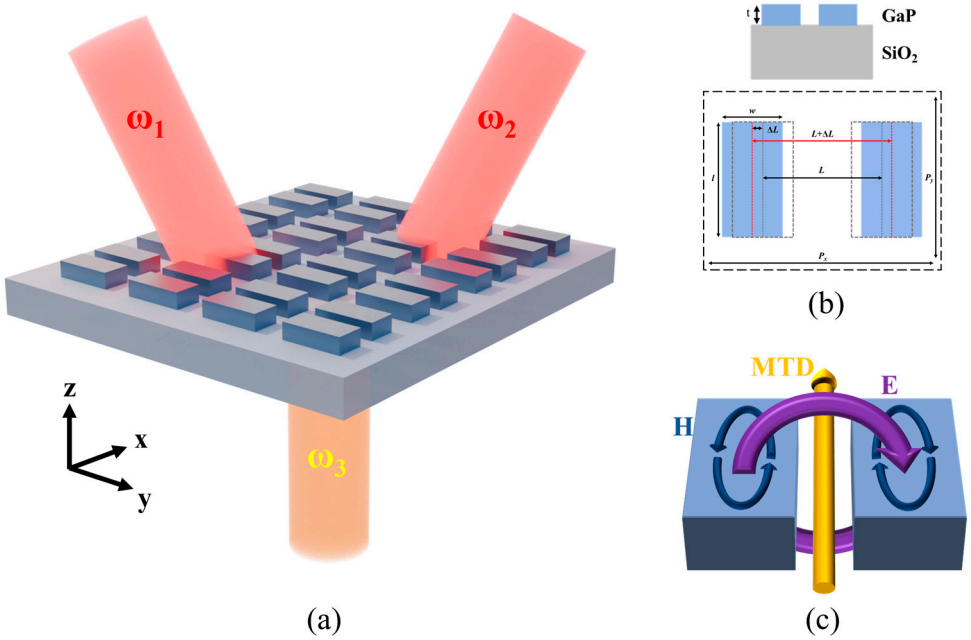


Figure 1. (**a**) Schematic of the metasurface; (**b**) Schematic of the metasurface structural parameters; (**c**) Schematic diagram of MTD.

The geometric parameters of the metasurface are meticulously defined as follows: the lattice periods are $P_x = 2255$ nm and $P_y = 1960$ nm. Each nanorod features a length of $l = 1180$ nm, a width of $w = 580$ nm, and a height of $t = 555$ nm. The refractive index of the SiO_2 substrate is set to $n_{SiO_2} = 1.46$, the refractive index of GaP is shown in the Supplementary Materials S1 [36]. The initial distance of the nanorod dimer is configured to half the lattice period, denoted as $L_0 = \frac{Px}{2} = 1127.5$ nm. The displacement from this central position is defined as $\Delta L = L - L_0$, which serves as the geometric asymmetry parameter. These parameters are indicated in Figure 1b.

Compared to a uniform array of single nanorods, the dimer metasurface physically achieves period doubling, which consequently shrinks the first Brillouin zone and folds the GMs back to the Γ point, which is initially located below the light line. When the center spacing of the two nanorods deviates from L_0 ($\Delta L \neq 0$), the in-plane translational symmetry of the unit cell is explicitly broken. This vital symmetry breaking enables the GMs folded at the Γ point to couple with the free-space radiative continuum, thereby exciting the MTD-QGM resonance mode with a high Q factor.

3. Results and Discussion

3.1. Analysis of the MTD Resonance Mode

First, we comprehensively investigated the band structure through numerical simulations using the finite element method software COMSOL Multiphysics 6.3. By applying Floquet periodic boundary conditions along both the x- and y-directions, we accurately modeled the infinite two-dimensional periodic structure. Eigenfrequency analysis was employed to calculate the Q factor of the resonance, defined as $Q = \omega_r/(2\omega_i)$, where ω_r and ω_i represent the real and imaginary parts of the complex eigenfrequency, respectively.

The simulated band structure of the metasurface is presented in Figure 2a. Due to Brillouin zone folding, modes originally situated below the light line are folded above it, generating QGM at the Γ point. Alongside the primary MTD-QGM of interest, two adjacent folded modes emerge. For clarity, we designate these as Mode A (the MTD-QGM), Mode B, and Mode C. Focusing first on Mode A, Figure 2b illustrates the evolution of its Q factor as a function of the transverse wave vector k_x at $\Delta L = 50$ nm, as well as its dependence on the asymmetry parameter ΔL. The Q factor exhibits exceptional stability in k-space, maintaining minimal fluctuations even across a broad range of wave vectors. Consequently, the resonance robustly preserves its high Q factor under varying angles of incidence.

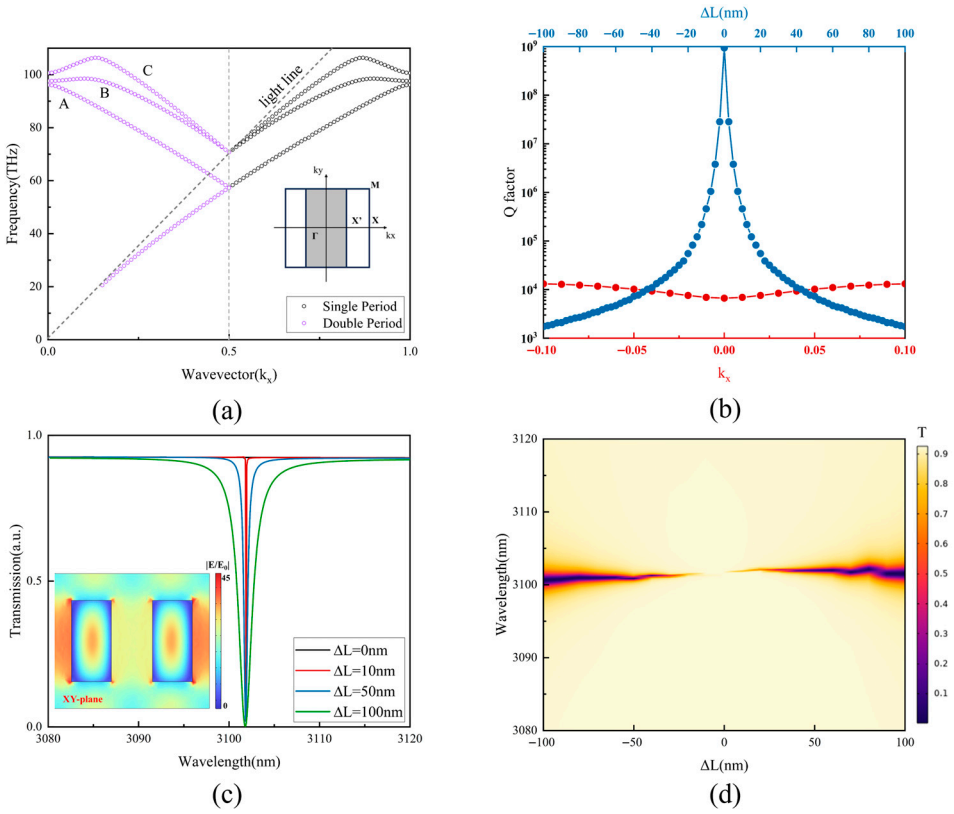


Figure 2. (**a**) Band diagram of the metasurface; (**b**) Variation of the Q factor as a function of k_x and ΔL (corresponding to the red dotted line and blue dotted line in the figure, respectively); (**c**,**d**) Relationship between the resonance wavelength and ΔL (the inset illustrates the localized enhancement of its electric field).

In contrast, the Q factor is strongly dependent on the nanorod spacing, degrading rapidly when the dimer gap deviates from a symmetric configuration. To realize a high Q MTD-QGM, we therefore fine-tuned the inter-rod distance. As depicted in Figure 2b, the Q factor and resonant wavelength are plotted against ΔL by blue line. The Q factor decreases significantly as ΔL increases, primarily due to the elevated radiative leakage induced by the broken structural symmetry. Notably, despite the varying ΔL, the resonant wavelength of the MTD-QGM remains remarkably stable around 3101.8 nm. To further corroborate the existence of the MTD-QGM, we mapped the transmittance of the metasurface under x-polarized illumination as a function of ΔL and resonant wavelength, as depicted in Figure 2d. Because the system maintains strict in-plane symmetry at $\Delta L = 0$ nm, the coupling between the mode folded at the Γ point and the free-space radiation field is strictly forbidden. Consequently, the resonance manifests as a GM. Thus, it is observed that the linewidth of the resonance peak in the transmission spectrum completely vanishes at $\Delta L = 0$ nm. As ΔL increases, the symmetry breaking opens the radiative channels, and the

resonance peak progressively broadens, signifying a reduction in the Q factor. For a clearer visualization of this trend, we extracted transmission spectra for three distinct ΔL values, shown in Figure 2c. Sharp Fano resonance peaks are clearly discernible near 3101.8 nm; as ΔL decreases, the spectral linewidth systematically narrows, ultimately disappearing at $\Delta L = 0$ nm. The inset of Figure 2c shows the field enhancement of the MTD-QGM at $\Delta L = 50$ nm. The electric field is highly confined within the GaP nanorod, reaching a maximum amplitude of approximately 35. This localized field enhancement provides favorable conditions for efficient nonlinear frequency conversion.

To further clarify the origin of the MTD-QGM, we analyze the Q factor distribution in *k*-space and the far-field polarization characteristics of the MTD-QGM. As shown in Figure 3a, The MTD-QGM possesses an infinite Q factor over a broad and continuous k_x range. Once in-plane structural asymmetry is introduced ($\Delta L > 0$), symmetry is broken across the entire band, allowing the GMs to couple to the free-space radiation continuum. Consequently, the Q factor is uniformly reduced throughout *k*-space, leading to the formation of the MTD-QGM.As shown in Figure 3b, the far-field polarization of the QGM evolves smoothly and trivially across momentum space, without any topological singularity. In contrast, the symmetry-protected bound state in the continuum (SP-BIC) exists only as a discrete state at the Γ point in k-space, where the Q factor diverges and drops rapidly away from Γ. Meanwhile, its far-field polarization exhibits a characteristic vortex-like singularity with a well-defined topological charge [29,30].

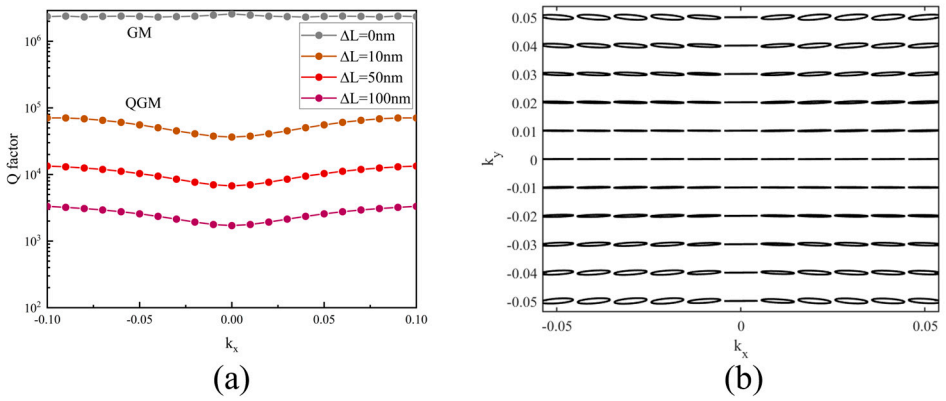


Figure 3. (**a**) Q factor distribution of the GM/QGM in *k*-space. (**b**) Far-field polarization of the MTD-QGM.

To quantitatively unravel the physical origin of the resonance peak, we performed a multipolar decomposition of the GaP nanorod dimer with an offset of $\Delta L = 50$ nm using the Cartesian multipole expansion method [37]. The specific formula can be found in the Supplementary Material S2. As illustrated in Figure 4a, the radiated power contributions from different multipole components vary significantly at the MTD-QGM resonant wavelength. The results dictate that the contribution of the MTD unequivocally dominates, with an intensity far surpassing those of the electric dipole (ED) and magnetic dipole (MD). Further analysis in conjunction with the radiation pattern in Figure 4b reveals that the MTD-QGM exhibits pronounced anisotropy, channeling electromagnetic energy primarily along the y-direction.

Moreover, comparing the near-field distributions of the magnetic and electric field vectors in Figure 4c,d corroborates the dominant MTD response. Specifically, Figure 4c displays that in the x-y plane, the magnetic field vectors form two opposing circular distributions, resembling a pair of anti-rotating magnetic vortices. This localized magnetic field configuration inherently induces head-to-tail electric dipole moments in the x-z plane, as shown in Figure 4d. Ultimately, this distinctive topological field configuration excites a robust MTD resonance oriented along the y-direction. Both the microscopic near-field

distribution and the macroscopic far-field radiation unambiguously confirm that this resonant mode is governed by the MTD response.

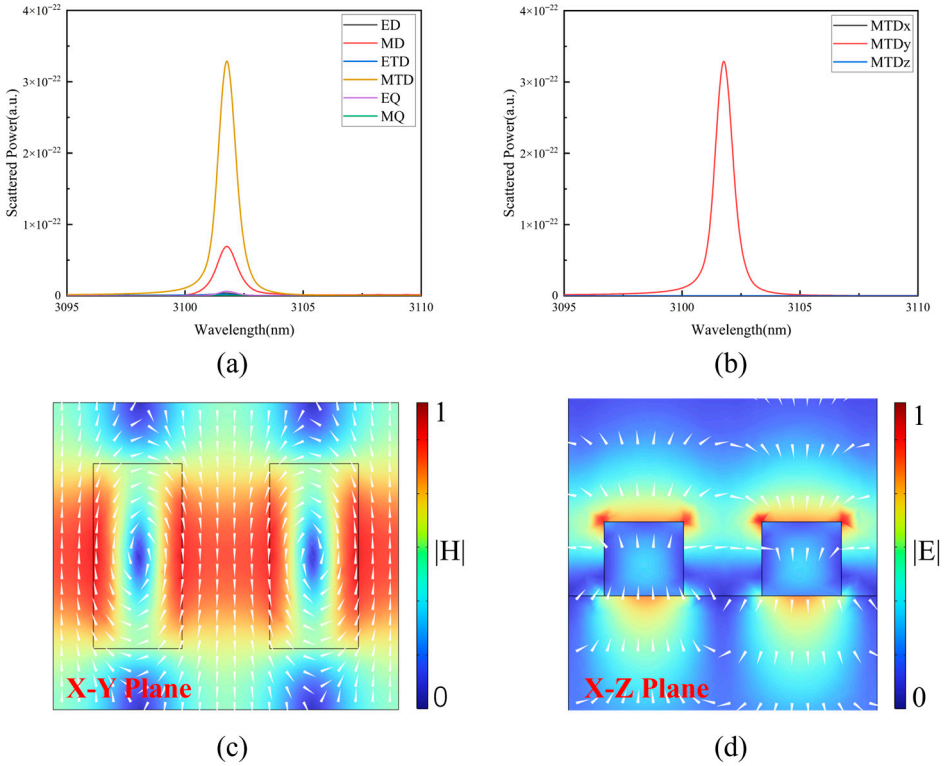


Figure 4. (**a**) Contributions from different multipoles in the multipole decomposition at $\Delta L = 50$ nm; (**b**) Components of MTD along the x, y, and z directions; (**c**) Distribution of normalized magnetic field vectors in the x-y plane; (**d**) Distribution of normalized electric field vectors in the x-y plane.

Additionally, we conducted a systematic analysis of the dispersion and near-field evolution of Mode B and Mode C, which reside adjacent to the dominant MTD-QGM. The simulation results indicate that, owing to distinct internal multipolar coupling mechanisms, these modes exhibit drastically different radiation characteristics in k-space. As shown in Figure 5, Mode B displays the typical traits of a strongly radiating "bright mode." The Q factor curve as a function of the transverse wavevector k_x in Figure 5a demonstrates that over a broad angular range of $-0.1 < k_x < 0.1$, the Q factor of Mode B remains at a relatively low level of 2000 to 4000 with an exceptionally flat profile. Further probing its near-field physical origin through the electric field amplitude and magnetic field amplitude distributions, as shown in Figure 5b,c, we find that the electric energy of Mode B is highly concentrated in the air gap between the two nanorods and at the outer edges of the structure. Simultaneously, the magnetic field is entirely localized within the GaP nanorods. In Supplementary Material S3, we confirm that this is the mode for y-polarized excitation. Due to the severe leakage of the electric field to the exterior of the structure, this field distribution profile makes Mode B unsuitable as an ideal resonance for efficient nonlinear upconversion.

In stark contrast, Mode C exhibits an unusual Q factor evolution in k-space. In the Q factor curve of Figure 5d, at Γ point, the Q factor is on the order of 10^5. However, with a minute angular deviation ($k_x \approx \pm 0.01$), the Q factor displays two extremely sharp peaks, surging to nearly 10^7. This phenomenon is a hallmark of an accidental bound state in the continuum (accidental BIC) or off-Γ BIC. According to the Friedrich–Wintgen interference theory [38,39], the electromagnetic waves radiated into the far field by two radiation channels undergo perfect destructive interference at specific angles, completely shutting

off the radiation. Combined with its near-field distribution, which is shown in Figure 5e,f, although the magnetic field of Mode C is strongly confined within the GaP nanorods, the magnetic vortex it sustains produces a closed-loop electric-field distribution that resides mainly in the air gaps rather than in the nonlinear medium, leading to limited modal overlap with the pump mode. Moreover, the Q factor distribution in k-space shows that a high Q factor is sustained only at a specific k_x, with strong sensitivity to any variation in k_x, in marked contrast to the robust Q factor bandwidth of the MTD-QGM. Consequently, Mode C is not an ideal resonance for broadband, tunable MIR upconversion.

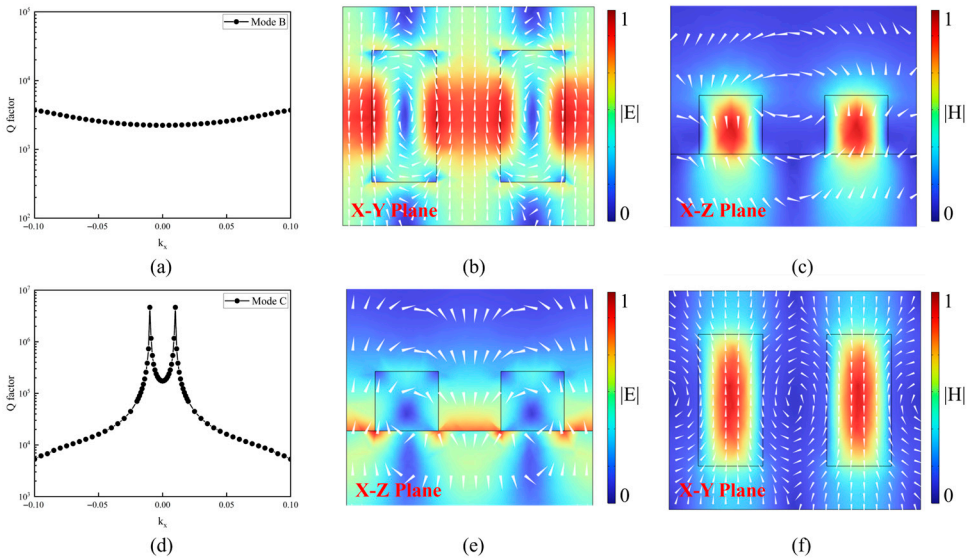


Figure 5. (**a**) Variation of the Q factor for Mode B in k-space; (**b**,**c**) Distribution of the electric field vector and magnetic field vector for Mode B; (**d**) Variation of the Q factor for Mode C in k-space; (**e**,**f**) Distribution of the electric field vector and magnetic field vector for Mode C.

Figure 6 illustrates the variation of the transmission spectrum of the MTD-QGM at different incident angles θ. The figure clearly shows that as the incident angle gradually increases, corresponding to an increase in the transverse wave vector k_x, the MTD resonance peak exhibits a pronounced red-shift trend. Analyzing this red-shifting trend alongside the previously mentioned Q factor stability in k space reveals the structure's outstanding integrated performance. Within an incidence-angle range of 0–10°, the MTD-QGM exhibits a tunable bandwidth of approximately 240 nm. Typically, QBICs modes protected by symmetry exhibit extreme sensitivity to incident angle, where even minor angular deviations often cause significant fluctuations in the Q factor. However, the unique feature of our designed GaP metasurface is that, despite the wavelength shift with angle, its Q factor consistently maintains a relatively high and stable magnitude. This simultaneous wavelength tunability and Q factor stability demonstrates the exceptional robustness of the MTD mode's localized field enhancement across k-space. Consequently, it establishes a crucial foundation for broadband MIR upconversion detection and imaging.

As a prototypical three-wave mixing nonlinear process, the ultimate conversion efficiency of SFG depends not only on the local enhancement of monochromatic fields but also, to a critical extent, on the precise spatial mode overlap between the interacting signal and pump beams. Driven by this underlying physical mechanism, we meticulously engineered the resonance characteristics of the pump beam. Figure 7a presents the transmission spectrum of the metasurface in the near-infrared regime, where we strategically selected the transmission dip at 1273.2 nm as the pump resonance mode.

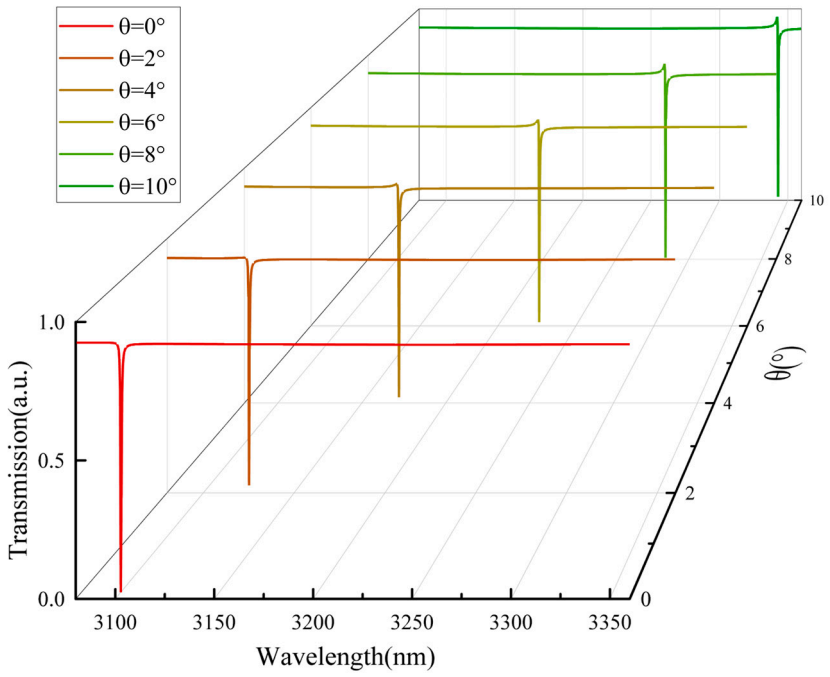


Figure 6. At $\Delta L = 50$ nm, Variation of the resonant wavelength of the MTD-QGM at incident angles of 0°, 2°, 4°, 6°, 8°, and 10°.

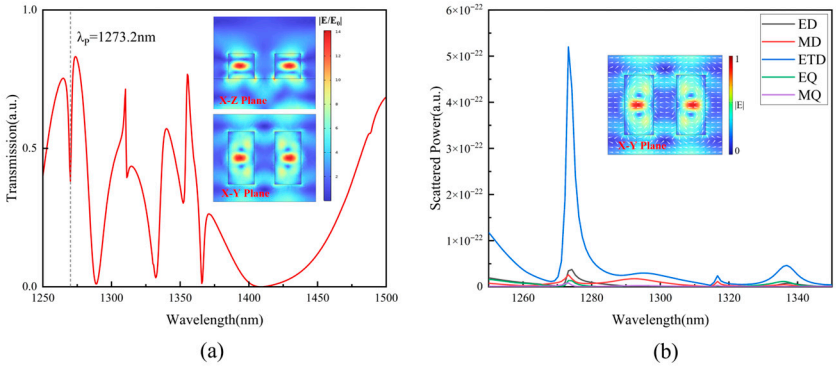


Figure 7. (**a**) Transmission spectrum of pump light (insets show electric field distributions in the x-z and x-y planes, respectively) at $\Delta L = 50$ nm; (**b**) Multilevel decomposition of pump resonance (inset shows electric field vector distribution).

Combined with the near-field electric distributions (x-z and x-y plane) in the inset of Figure 7a, it is evident that the enhanced electric field excited by the pump light is also highly localized within the GaP nanorod dimers. This field distribution achieves an exceptional spatial overlap with the aforementioned high Q MTD mode of the signal light confined entirely within the dielectric, providing a highly favorable prerequisite for highly efficient nonlinear interactions.

To further elucidate the physical origin of this pump resonance, we conducted a multipole expansion analysis. As depicted in Figure 7b, at the 1273.2 nm resonance, the response is overwhelmingly dominated by the ETD oriented along the x-direction. From the electromagnetic vector distribution in the inset of Figure 7b, a pair of anti-rotating displacement current vortices is excited inside the nanorod dimer. These vortex currents subsequently induce magnetic dipole moments aligned along the $\pm z$ directions, which eventually connect head-to-tail to form a robust x-directed toroidal dipole resonance. This distinctive topological current distribution further ensures the rigid confinement of the pump electromagnetic energy entirely within the nonlinear dielectric.

Before analyzing the nonlinear frequency-conversion process in detail, it is essential to first verify the experimental feasibility and structural robustness of the proposed GaP metasurface. Although the present study is primarily concerned with theoretical design and numerical evaluation, we systematically examine the fabrication tolerance of the GaP nanorod dimer. Extensive parameter sweeps indicate that typical geometric deviations lead to a highly predictable linear shift of the resonance wavelength, while the Q factor characteristics of both the MTD-QGM and the pump mode remain largely robust. A quantitative analysis of the geometric tolerances is given in the Supplementary Material S4. Such structural robustness provides a solid practical basis for the subsequent nonlinear upconversion simulations.

3.2. Nonlinear Sum-Frequency Generation

Subsequently, we numerically investigated the nonlinear SFG process within the proposed architecture at $\Delta L = 50$ nm. This process can be accurately evaluated through coupled electromagnetic models in sequential steps under the undepleted pump approximation. It is worth noting that the undepleted pump approximation is justified when the generated nonlinear signal is weak compared with the incident field, because the generated SFG power accounts for only a negligible fraction of the input power, such that the fundamental field can be regarded as constant throughout the entire interaction volume. Initially, the first and second electromagnetic models are simulated at the respective input wavelengths to obtain the local field distributions and compute the induced nonlinear polarization within the GaP active material. Subsequently, this polarization term is applied as the sole driving source in the third electromagnetic model at the sum-frequency wavelength, yielding the generated photon power flux propagating toward the substrate. As a III-V semiconductor, GaP possesses a non-centrosymmetric zinc-blende crystal structure and an exceptionally high second-order nonlinear susceptibility of $\chi^{(2)} \approx 70.6$ pm/V [40]. All simulations are performed using GaP oriented along the (110) crystallographic direction. The nonlinear polarization formula for (110)-GaP is provided in the Supplementary Material S5.

For the nonlinear simulations of the metasurface, we assume excitation by a femtosecond laser with a pulse duration of 150 fs and a repetition rate of 80 MHz. The input intensities of the signal and pump beams were set to 30 MW/cm^2 and 50 MW/cm^2, respectively. The SFG conversion efficiency was then calculated by integrating the Poynting vector over the output plane on the transmission side. The SFG conversion efficiency is defined as $\eta_{\mathrm{SFG}} = P_{\mathrm{SFG}}/P_s$, where P_{SFG} is the output power of the generated SFG signal and P_s is the input power of the incident signal beam. Since the SFG signal generated by our metasurface is emitted predominantly in the $+z$ direction, whereas the conversion efficiency in the $-z$ direction is less than half of that in the forward direction, as shown in the Supplementary Material S6, all conversion efficiencies discussed in the nonlinear simulations refer to the forward conversion efficiency.

By tuning the wavelengths of the signal and pump beams around the spectral region of interest, the SFG conversion efficiency was systematically evaluated. As shown in Figure 8, the SFG process exhibits a strong dependence on the input wavelengths. We calculated the SFG efficiency while sweeping the signal wavelength λ_s around the resonance zone, with the pump wavelength λ_p securely fixed at 1273.2 nm. The calculated spectrum is shown in Figure 8a. A maximum conversion efficiency of $\eta_{\mathrm{SFG}} = 7.9 \times 10^{-4}$ is observed at $\lambda_s = 3101.8$ nm, which translates to an SFG signal generated around 903 nm. Next, we calculated the SFG efficiency while varying the pump beam wavelength from 1265 nm to 1280 nm, keeping λ_s fixed at 3101.8 nm. The resulting SFG spectrum, depicted in Figure 8b, reveals that the maximum SFG conversion efficiency unequivocally occurs at a pump wavelength of 1273.2 nm. We have added a table in Supplementary Material S7 to provide

a detailed comparison of other SFG metasurfaces. This sharp peak is a direct consequence of the ultra-high Q factor of the MTD-QGM, which yields an extremely narrow resonance bandwidth. The maximum SFG enhancement demonstrates excellent agreement with the spectral positions of the resonances. To confirm that the observed high SFG efficiency is indeed driven by the MTD-QGM, we compare the GaP metasurface with an unpatterned GaP film. As shown in Figure 8c, the metasurface exhibits an SFG conversion efficiency that is 6×10^8 times higher than that of the unpatterned film, confirming the critical role of the MTD-QGM in enhancing the SFG process.

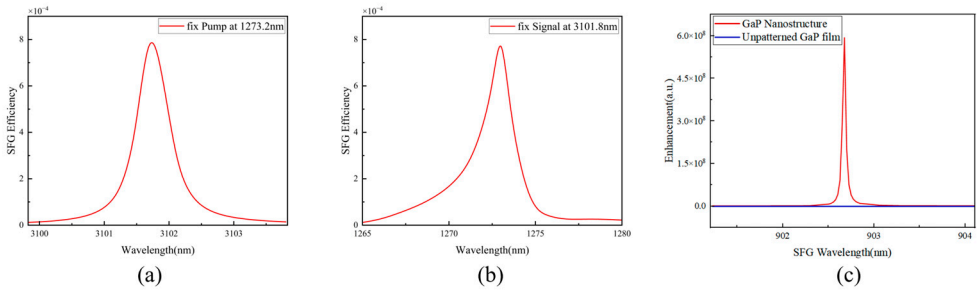


Figure 8. Variation of the SFG conversion efficiency. (**a**) Dependence on the signal wavelength while fixing the pump wavelength; (**b**) Dependence on the pump wavelength while fixing the signal wavelength; (**c**) Comparison of the conversion efficiency between the GaP nanostructure and the unpatterned GaP film.

Capitalizing on the remarkably robust high-Q nature of the MTD-QGM across a broad wavevector range, the proposed metasurface offers an effective mechanism to overcome the inherent narrow-band limitations typical of QBICs. Figure 9a presents the normalized intensity of the SFG signal generated in the near-infrared band under varying incident angles. It should be noted that, for any single fixed angle of incidence, the significant enhancement of SFG efficiency is confined to a strictly narrow spectral range, which is a fundamental hallmark of high Q resonances. However, benefiting from the exceptional *k*-space stability of the MTD-QGM, as the incident angle varies, the resonant wavelength smoothly tunes while the peak intensity of the sum-frequency signal remains at consistently high levels. It can also be observed from the figure that the peak SFG intensity at normal incidence ($\theta = 0°$) is marginally lower than that at oblique incidence ($\theta \neq 0°$); this is primarily attributed to the slightly lower Q factor at $k_x = 0$ compared to $k_x \neq 0$.

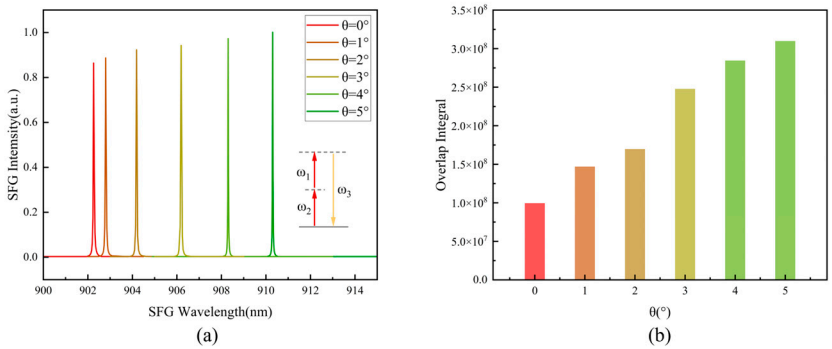


Figure 9. (**a**) Normalized intensity of SFG signals at different incident angles; (**b**) Overlap integral at different incident angles.

We further investigated the causes of this phenomenon by calculating the mode field overlap integral at different angles. The formula for the mode field overlap integral is as follows:

$$\eta \propto |\int_V \chi^{(2)} : E_{Signal}(\omega_S) E_{pump}(\omega_P) \cdot E^*_{SFG}(\omega_{SFG}) dV|^2$$

The overlap integral represents the tendency for energy to flow from the signal and pump optical modes to the frequency-converted optical mode, and this integral is performed over the volume V of the nonlinear medium. The results are shown in Figure 9b, where it can be observed that the value of the overlap integral increases with the incident angle. This further explains the enhanced conversion efficiency under oblique incidence. It should be noted that the units of the overlapping integral are not important; we are only comparing the magnitudes of the overlapping integral at different incident angles. Additionally, we defined an electric field enhancement factor to further explain this phenomenon, as detailed in Supplementary Material S8. In summary, by continuously adjusting the incident angle of the signal beam, the designed metasurface can dynamically tune its operational wavelength without sacrificing conversion efficiency, thereby enabling a continuous, broadband, and highly efficient sum-frequency output.

To rigorously verify that the generated signal originates from the SFG process rather than competing nonlinear optical effects, we analyzed the power dependence of the emission. As illustrated in Figure 10a, the scaling of the SFG power density with respect to the incident signal and pump power densities is plotted on a logarithmic (log-log) scale. The discrete data points perfectly fit the solid red and orange lines, both of which exhibit a slope strictly equal to 1. This characteristic clearly distinguishes SFG from second-harmonic generation (slope = 2) or third-harmonic generation (slope = 3). This linear response unambiguously proves that the newly generated photons in the system are co-upconverted by one signal photon and one pump photon, governed by the energy conservation mechanism $\omega_{\mathrm{SFG}} = \omega_{\mathrm{signal}} + \omega_{\mathrm{pump}}$.

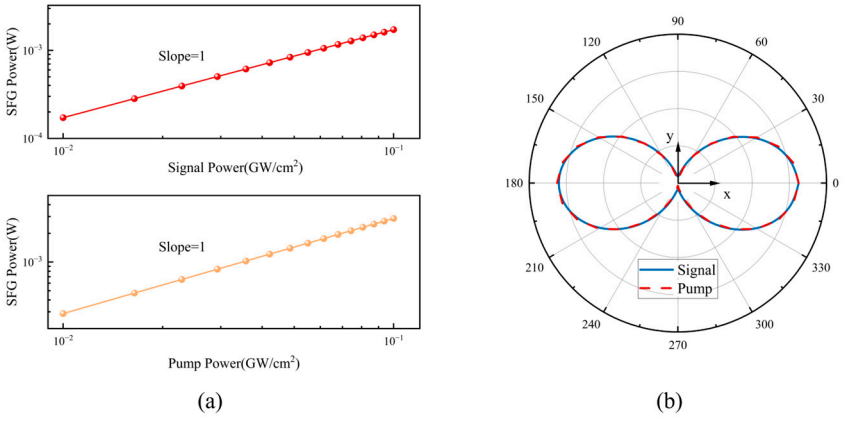


Figure 10. (**a**) Relationship between SFG power and average pump power density at the resonant wavelength; (**b**) Dependence of the SFG process on signal and pump polarization.

To conclude our analysis, we systematically investigated how the polarization states of the excitation beams influence the SFG intensity. In these calculations, the operating wavelengths were fixed at λ_s = 3101.8 nm and λ_p = 1273.2 nm. We first varied the polarization angle of the signal beam while maintaining a strictly x-polarized pump beam. As illustrated by the solid blue curve in Figure 10b, the maximum SFG emission occurs when the signal is polarized at 0°. In a complementary analysis, the signal polarization was fixed at 0° while the pump polarization angle was varied. As illustrated by the dashed red line in Figure 10b, the peak SFG in this configuration is similarly obtained with an x-polarized pump beam. This strong polarization anisotropy originates fundamentally from two physical mechanisms: first, the geometric topology of the designed GaP nanorod dimers breaks the rotational symmetry in the x-y plane, dictating that the supported MTD-QGM and

pump resonance modes can only be efficiently excited by electric fields with specific polarization components; second, the inherent $\bar{4}3m$ point-group symmetry of the GaP crystal strictly modulates the non-zero elements of its $\chi^{(2)}$ tensor based on the crystallographic orientation. These results demonstrate that x-polarized incident light optimally leverages both the localized field enhancement of the metasurface and the nonlinear polarization components of the material, thereby maximizing the sum-frequency emission.

4. Discussions

In summary, we have theoretically proposed and numerically demonstrated an all-dielectric GaP metasurface that enables highly efficient MIR nonlinear upconversion, driven by a high Q MTD-QGM. By strategically introducing an in-plane geometric asymmetry (ΔL) to the GaP nanorod dimers, we successfully excited the MTD-QGM. This mode not only exhibits exceptional Q factor robustness in k-space but also tightly confines the strongly enhanced near-fields entirely within the dielectric structures. Leveraging this highly stable high Q resonance in conjunction with a precisely mode-matched pump resonance, we achieved a remarkable SFG conversion efficiency of 7.9×10^{-4}, effectively translating a MIR signal at 3101.8 nm into the near-infrared band around 903 nm. Crucially, the outstanding k-space stability of the MTD-QGM intrinsically overcomes the strict narrow-band limitations typical of symmetry-protected resonances, enabling continuous, broadband upconversion output by simply tuning the angle of incidence without sacrificing conversion efficiency. Furthermore, the strong polarization dependence of the SFG emission provides an additional degree of freedom for nonlinear light manipulation. Our findings not only advance the fundamental understanding of high Q multipolar physics but also pave the way for robust, room-temperature MIR detection, coherent light sources, and advanced nonlinear optical imaging technologies.

Supplementary Materials: The following supporting information can be downloaded at: https://www.mdpi.com/article/10.3390/photonics13040350/s1, Figure S1: Refractive index of GaP; Figure S2: (a) Resonant transmission spectrum under y-polarization; (b) Distribution of electric field vectors under y-polarization; Distribution of magnetic field vectors under y-polarization; Figure S3: Fabrication-tolerance analysis of the signal mode; Figure S4: Fabrication-tolerance analysis of the pump mode; Figure S5: Comparison of the forward and backward conversion efficiencies of the metasurface; Figure S6: (a–f) shows the electric field enhancement factors for incident angles of 0°, 1°, 2°, 3°, 4°, and 5°, respectively; Table S1: Tolerance of structural parameters of nanorods; Table S2: Comparison of SFG conversion efficiency in different nanostructures.

Author Contributions: Conceptualization, W.Z. and C.Z.; methodology, W.Z.; investigation, W.S.; writing—original draft preparation, W.Z.; writing—review and editing, W.Z., C.Z. and D.M.; project administration, H.L.; funding acquisition, H.L. All authors have read and agreed to the published version of the manuscript.

Funding: This research was funded by the National Natural Science Foundation grant number 61975232.

Institutional Review Board Statement: Not applicable.

Informed Consent Statement: Not applicable.

Data Availability Statement: Data underlying the results presented in this paper are not publicly available at this time but may be obtained from the authors upon reasonable request.

Conflicts of Interest: The authors declare no conflicts of interest.

References

1. Rothman, L.S.; Gordon, I.E.; Babikov, Y.; Barbe, A.; Benner, D.; Bernath, P.F.; Birk, M.; Bizzocchi, L.; Boudon, V.; Brown, L.R.; et al. The HITRAN2012 molecular spectroscopic database. *J. Quant. Spectrosc. Radiat. Transf.* **2013**, *130*, 4–50. [CrossRef]

2. Hodgkinson, J.; Tatam, R.P. Optical gas sensing: A review. *Meas. Sci. Technol.* **2013**, *24*, 012004. [CrossRef]
3. Fang, J.; Huang, K.; Qin, R.; Liang, Y.; Wu, E.; Yan, M.; Zeng, H. Wide-field mid-infrared hyperspectral imaging beyond video rate. *Nat. Commun.* **2024**, *15*, 1811. [CrossRef] [PubMed]
4. Rogalski, A.; Chrzanowski, K. Infrared devices and techniques. In *Handbook of Optoelectronics*; CRC Press: Boca Raton, FL, USA, 2017; pp. 633–686.
5. Boyd, R.W.; Gaeta, A.L.; Giese, E. Nonlinear optics. In *Springer Handbook of Atomic, Molecular, and Optical Physics*; Springer International Publishing: Cham, Switzerland, 2008; pp. 1097–1110.
6. Bin-Alam, M.S.; Reshef, O.; Mamchur, Y.; Alam, M.Z.; Carlow, G.; Upham, J.; Sullivan, B.T.; Menard, J.M.; Huttunen, M.J.; Boyd, R.W.; et al. Ultra-high-Q resonances in plasmonic metasurfaces. *Nat. Commun.* **2021**, *1*, 974. [CrossRef] [PubMed]
7. Sain, B.; Meier, C.; Zentgraf, T. Nonlinear optics in all-dielectric nanoantennas and metasurfaces: A review. *Adv. Photonics* **2019**, *1*, 024002. [CrossRef]
8. Gao, S.; Wang, Z.; Lu, N.; Xu, L.; Han, Z.; Rahmani, M.; Jia, Y.; Chen, F. Lithium tantalate resonant metasurfaces for highly efficient ultraviolet harmonic generation. *Appl. Phys. Rev.* **2025**, *12*, 031404. [CrossRef]
9. Jain, A.; Moitra, P.; Koschny, T.; Valentine, J.; Soukoulis, C.M. Electric and magnetic response in dielectric dark states for low loss subwavelength optical meta atoms. *Adv. Opt. Mater.* **2015**, *3*, 1431–1438. [CrossRef]
10. Li, G.; Zhang, S.; Zentgraf, T. Nonlinear photonic metasurfaces. *Nat. Rev. Mater.* **2017**, *2*, 17010. [CrossRef]
11. del Rocio Camacho-Morales, M.; Rocco, D.; Xu, L.; Gili, V.F.; Dimitrov, N.; Stoyanov, L.; Ma, Z.; Komar, A.; Lysevych, M.; Karouta, F.; et al. Infrared upconversion imaging in nonlinear metasurfaces. *Adv. Photonics* **2021**, *3*, 036002. [CrossRef]
12. Carletti, L.; Locatelli, A.; Stepanenko, O.; Leo, G.; De Angelis, C. Enhanced second-harmonic generation from magnetic resonance in AlGaAs nanoantennas. *Opt. Express* **2015**, *23*, 26544–26550. [CrossRef]
13. Carletti, L.; Locatelli, A.; Neshev, D.; De Angelis, C. Shaping the radiation pattern of second-harmonic generation from AlGaAs dielectric nanoantennas. *ACS Photonics* **2016**, *3*, 1500–1507. [CrossRef]
14. Papasimakis, N.; Fedotov, V.A.; Savinov, V.; Raybould, T.A.; Zheludec, N.I. Electromagnetic toroidal excitations in matter and free space. *Nat. Mater.* **2016**, *15*, 263–271. [CrossRef]
15. Ahmadivand, A.; Gerislioglu, B.; Ahuja, R.; Mishra, Y.K. Toroidal metaphotonics and metadevices. *Laser Photonics Rev.* **2020**, *14*, 1900326. [CrossRef]
16. Zheng, Z.; Rocco, D.; Ren, H.; Sergaeva, O.; Zhang, Y.; Whaley, K.B.; Ying, C.; Ceglia, D.D.; De-Angelis, C.; Rahmani, M.; et al. Advances in nonlinear metasurfaces for imaging, quantum, and sensing applications. *Nanophotonics* **2023**, *12*, 4255–4281. [CrossRef]
17. Hail, C.U.; Michaeli, L.; Atwater, H.A. Third harmonic generation enhancement and wavefront control using a local high-Q metasurface. *Nano Lett.* **2024**, *24*, 2257–2263. [CrossRef] [PubMed]
18. Jeong, J.; Goldflam, M.D.; Campione, S.; Briscoe, J.L.; Vabishchevich, P.P.; Nogan, J.; Sinclair, M.B.; Luk, T.S.; Brener, I. High quality factor toroidal resonances in dielectric metasurfaces. *ACS Photonics* **2020**, *7*, 1699–1707. [CrossRef]
19. Zong, X.; Li, L.; Liu, Y. Mirror-coupled toroidal dipole bound states in the continuum for tunable narrowband perfect absorption. *Opt. Laser Technol.* **2024**, *169*, 110144. [CrossRef]
20. Li, J.; Ma, T. Magnetic toroidal dipole resonances with high quality factor in all-dielectric metamaterial. *Opt. Commun.* **2022**, *507*, 127621. [CrossRef]
21. Cui, C.; Yuan, S.; Qiu, X.; Zhu, L.; Wang, Y.; Li, Y.; Song, J.; Huang, Q.; Zeng, C.; Xia, J. Light emission driven by magnetic and electric toroidal dipole resonances in a silicon metasurface. *Nanoscale* **2019**, *11*, 14446–14454. [CrossRef]
22. Koshelev, K.; Tang, Y.; Li, K.; Choi, D.Y.; Li, G.; Kivshar, Y. Nonlinear metasurfaces governed by bound states in the continuum. *ACS Photonics* **2019**, *6*, 1639–1644. [CrossRef]
23. Koshelev, K.; Lepeshov, S.; Liu, M.; Bogdanov, A.; Kivshar, Y. Asymmetric metasurfaces with high-Q resonances governed by bound states in the continuum. *Phys. Rev. Lett.* **2018**, *121*, 193903. [CrossRef]
24. Jiang, X.; Luo, M.; Zhang, Z.; You, J.; Lan, Z. Quasi-flatband resonances and bound states in the continuum in coupled photonic topological defects for boosting light–matter interactions. *Chin. Opt. Lett.* **2025**, *23*, 103602. [CrossRef]
25. Wang, J.; Xu, H.; Si, J.; Wu, H.; Wang, H.; Qiu, H.; Jiang, H.; Qin, M.; Liu, J.; Wu, F.; et al. Chirality inversion for tailoring light generation in nonlinear van der Waals metasurfaces. *Appl. Phys. Lett.* **2025**, *127*, 061701. [CrossRef]
26. Dong, A.; Zhu, Y.; Wu, H.; Wang, J.; Qin, M.; Liu, J.; Wu, F.; Li, H. Photonic-spin-controlled second-order nonlinear frequency conversion on permittivity-asymmetry lithium niobite dimer metasurfaces governed by chiral quasibound states in the continuum. *Phys. Rev. B* **2025**, *111*, 075301. [CrossRef]
27. Zhang, B.; Dong, A.; Qin, M.; Liu, J.; Qiu, J.; Xiao, S.; Huang, W.; Li, H. Wavelength-Locked Quasi-BICs for Enhanced Third-Harmonic Generation in Silicon Metasurfaces. *Adv. Opt. Mater.* **2026**, *14*, e03449. [CrossRef]
28. Sun, K.L.; Wei, H.; Chen, W.J.; Chen, Y.; Cai, Y.J.; Qiu, C.W.; Han, Z.H. Infinite-Q guided modes radiate in the continuum. *Phys. Rev. B* **2023**, *107*, 115415. [CrossRef]
29. Sun, K.; Wang, W.; Han, Z. High-Q resonances in periodic photonic structures. *Phys. Rev. B* **2024**, *109*, 085426. [CrossRef]

30. Jiang, H.; Sun, K.; Jia, Y.; Cai, Y.; Levy, U.; Han, Z. Tunable second harmonic generation with large enhancement in a nonlocal all-dielectric metasurface over a broad spectral range. *Adv. Opt. Mater.* **2024**, *12*, 2303229. [CrossRef]
31. Wang, W.; Srivastava, Y.K.; Tan, T.C.; Wang, Z.; Singh, R.J. Brillouin zone folding driven bound states in the continuum. *Nat. Commun.* **2023**, *14*, 2811. [CrossRef]
32. Duan, H.; He, H.; Yi, Y.; Wang, L.; Zhang, Y.; You, S.; Wang, Y.; Gao, C.G.; Huang, J.; Zhou, C. Efficient second-harmonic generation in a lithium niobate metasurface governed by high-Q magnetic toroidal dipole resonances. *Opt. Lett.* **2024**, *49*, 5539–5542. [CrossRef]
33. Cambiasso, J.; Grinblat, G.; Li, Y.; Rakovich, A.; Cortés, E.; Maier, S.A. Bridging the gap between dielectric nanophotonics and the visible regime with effectively lossless gallium phosphide antennas. *Nano Lett.* **2017**, *17*, 1219–1225. [CrossRef]
34. Wilson, D.J.; Schneider, K.; Hönl, S.; Anderson, M.; Kippenberg, T.J.; Seidler, P. Integrated gallium phosphide nonlinear photonics. *Nat. Photonics* **2020**, *14*, 57–62. [CrossRef]
35. Camacho-Morales, R.; Xu, L.; Zhang, H.; Ha, S.T.; Krivitsky, L.; Kuznetsov, A.I.; Rahmani, M.; Neshev, D. Sum-frequency generation in high-Q GaP metasurfaces driven by leaky-wave guided modes. *Nano Lett.* **2022**, *22*, 6141–6148. [CrossRef] [PubMed]
36. Adachi, S. Optical dispersion relations for GaP, GaAs, GaSb, InP, InAs, InSb, $Al_xGa_{1-x}As$, and $In_{1-x}Ga_xAs_yP_{1-y}$. *J. Appl. Phys.* **1989**, *66*, 6030–6040. [CrossRef]
37. Yang, Z.; Deng, Y.; Yu, Y.; He, J. Magnetic toroidal dipole response in individual all-dielectric nanodisk clusters. *Nanoscale* **2020**, *12*, 10639–10646. [CrossRef]
38. Friedrich, H.; Wintgen, D. Interfering resonances and bound states in the continuum. *Phys. Rev. A* **1985**, *32*, 3231. [CrossRef]
39. Hsu, C.W.; Zhen, B.; Stone, A.D.; Joannopoulos, J.D.; Soljačić, M. Bound states in the continuum. *Nat. Rev. Mater.* **2016**, *1*, 16048. [CrossRef]
40. Pomeranz, L.A.; Schunemann, P.G.; Magarrell, D.J.; McCarthy, J.C.; Zawilski, K.T.; Zelmon, D.E. 1-micron-pumped OPO based on orientation-patterned GaP. In *Proceedings of the Nonlinear Frequency Generation and Conversion: Materials, Devices, and Applications XIV, San Francisco, CA, USA, 7–12 February 2015*; SPIE: Bellingham, WA, USA, 2015; Volume 9347, pp. 129–135.

Disclaimer/Publisher's Note: The statements, opinions and data contained in all publications are solely those of the individual author(s) and contributor(s) and not of MDPI and/or the editor(s). MDPI and/or the editor(s) disclaim responsibility for any injury to people or property resulting from any ideas, methods, instructions or products referred to in the content.